

# Detecting WIMPs in the Microwave Sky

P. BLASI<sup>1</sup>, A. V. OLINTO<sup>2,3</sup>, and C. TYLER<sup>2</sup>

<sup>1</sup>INAF/Osservatorio Astrofisico di Arcetri, Largo Enrico Fermi, 5 - 50125 Firenze, ITALY

<sup>2</sup>Department of Astronomy & Astrophysics and Enrico Fermi Institute, The University of Chicago, Chicago, IL 60637, USA

<sup>3</sup>Center for Cosmological Physics, The University of Chicago, Chicago, IL 60637, USA

**Abstract.** The hierarchical clustering observed in cold dark matter simulations results in highly clumped galactic halos. If the dark matter in our halo is made of weakly interacting massive particles (WIMPs), their annihilation products should be detectable in the higher density and nearby clumps. We consider WIMPs to be neutralinos and calculate the synchrotron flux from their annihilation products in the presence of the Galactic magnetic field. We derive a self-consistent emission spectrum including pair annihilation, synchrotron self-absorption, and synchrotron self-Compton reactions. The resulting radiation spans microwave frequencies that can be observed over the anisotropies in the cosmic microwave background. These synchrotron sources should be identifiable as WIMP clumps, either by their spatial structure or by their distinctive radio spectrum.

## 1 Introduction

The density of dark matter in the Universe is observed via its gravitational effects on galaxies and clusters of galaxies to constitute about 30% of the critical density of the Universe. The nature of this dominant matter component is still unknown. Primordial nucleosynthesis and acoustic peaks in the cosmic microwave background (CMB) constrain the density of baryonic matter to be less than about 5% of the critical density, thus most of the dark matter is non-baryonic. The leading candidate for the dark matter is the lightest supersymmetric particle in supersymmetric extensions of the standard model that can be stable by conservation of R-parity. In most scenarios this weakly interacting massive particle (WIMP) is the neutralino,  $\chi$ , which is a linear combination of the photino, the zino, and the higgsinos (for a review, see Jungman, Kamionkowski and Griest (1996)).

Neutralinos may be detected directly as they traverse the Earth or indirectly by the observation of their annihilation products. Direct neutralino searches are now underway in a number of low temperature experiments with no consensus detection as of yet. Indirect searches have been proposed both for gamma rays and synchrotron emission from the annihilation of WIMPs in the Galactic center (Berezinsky, Gurevich, and Zybin, 1992; Berezinsky, Bottino, and Mignola, 1994). The rate of neutralino annihilation is proportional to the neutralino density squared ( $\sim n_\chi^2$ ), therefore the strongest flux is expected to come from the highest density regions such as the Galactic center. Depending on the history of formation of the central black hole in our Galaxy,

the WIMP density may be strongly enhanced in the neighborhood of the black hole. The density enhancement coupled with assumptions about the local strength of the magnetic field can, in principle, constrain viable models for neutralino masses and cross sections (Gondolo and Silk, 1999; Gondolo, 2000).

Although promising, the proposal to focus indirect searches on the Galactic nucleus is not free of uncertainties. The presence of central cusps in large halos has been questioned by observations Salucci (2000). In addition, the large fraction of baryonic matter as well as the history of the central black hole are likely to alter the dynamics of the dark matter in the Galactic center. Major mergers in the central black hole's past will tend to decrease the dark matter density. A clear picture of the magnetic structure around a central black hole is also lacking. In addition, when the neutralino density becomes very high, the synchrotron signature is strongly modified by synchrotron self-Compton scatterings and pair annihilation, as we discuss below and in (Aloisio et al., 2002a). A cleaner dark matter annihilation signal may be detected against a better understood background using the clumpy nature of our halo.

Superimposed on the smooth component of CDM halos, high-resolution simulations find a large degree of substructure formed by the constant merging of smaller halos to form a present dark matter halo (see, for example, Ghigna et al. (1998)). The large number of clumps generated through the hierarchical clustering of CDM comprises about 10 – 20% of the total mass of a given halo. High density and nearby clumps in our own halo enhance appreciably the emission of gamma rays and neutrinos from neutralino annihilation (Bergström et al., 1999; Calcáneo-Roldán and Moore, 2001). As these clumps reach closer to the Galactic plane, the Galactic magnetic field strength increases drastically and the synchrotron signal from the charged products of neutralino annihilation intensifies considerably.

Here, we calculate in detail the synchrotron radiation of electrons and positrons generated as decay products of WIMP annihilation in the Galactic magnetic field. We show that the synchrotron emission can provide a crucial test of WIMP models, since the predicted fluxes are in the microwave region and exceed the signal of CMB anisotropies at some frequencies. The detection of this excess radiation from small angular size regions in the sky may provide the first signal of WIMP dark matter.

In section 2, we explain the calculation procedure. In sections 3 and 4 we present results for two different clump den-

sity profiles. Section 5 is the conclusion, with prospects for detection.

## 2 Synchrotron from Dark Matter Clumps

### 2.1 Dark Matter Clump Structure

The density profile of dark matter halos has yet to be precisely determined. The possible profiles for the smooth dark matter component on the scales of galaxies is reasonably well constrained by observations of galactic dynamics together with CDM simulations. In contrast, the structure of the smaller dark matter halos (i.e., clumps) is only constrained by theoretical arguments and numerical simulations. Our Galactic halo can be described by both a smooth large scale component plus a distribution of clumps which are the smaller halos that have fallen into the Galactic potential well as it formed from lower mass objects.

In order to derive the synchrotron emission from neutralino annihilation in the dark matter clumps of our Galaxy, we need to model both the smooth component of the halo as well as the individual density profile of the clumps. We consider the halo of the Galaxy to be well described by the Navarro, Frenk, and White (NFW) density profile (Navarro, Frenk and White, 1996, 1997) which we describe below. We model the individual clumps of dark matter in our halo by two choices of CDM halo profiles that span the range of reasonable slopes: the NFW profile and the singular isothermal sphere (SIS). These two models bracket a range of possible clump density profiles.

The NFW profile arises from CDM simulations and is consistent with observations of a number of galaxies. The dark matter density as a function of radius from the center of the particular halo is given by:

$$\rho(r) = m_\chi n_0 \left(\frac{r}{r_c}\right)^{-1} \left[1 + \frac{r}{r_c}\right]^{-2}, \quad (1)$$

where  $r_c$  is a core radius and  $m_\chi$  is the neutralino mass. This profile gives a broad core region with a gently sloping profile inside ( $\rho \sim r^{-1}$ ) and a steeper slope outside  $r_c$  ( $\rho \sim r^{-3}$ ). In general,  $n_0$  and  $r_c$  are fixed by the total mass of the halo inside some radius  $R_{\text{halo}} \gg r_c$  and the density at some particular point (or equivalently the velocity dispersion at that point). To set these parameters for the smooth component of our Galactic halo, we chose  $r_c = R_{\text{halo}}/10$  where  $R_{\text{halo}}$  is the radius within which lies most of our halo's mass,  $M_{\text{halo}}(r \leq R_{\text{halo}}) = 2 \times 10^{12} M_\odot$ . In addition, we set the density in the solar neighborhood from the local velocity dispersion to be  $\rho_\odot \equiv \rho(8.5 \text{ kpc}) = 6.5 \times 10^{-25} \text{ g/cm}^3$  which fixes all parameters.

For each individual clump described by the NFW profile, we fix  $r_c$  and  $n_0$  by setting  $r_c = R_c/10$  where  $R_c$  is the radius at which the density of the clump equals that of the smooth host halo density. The total mass of the clump is then determined by the mass inside  $R_c$ .

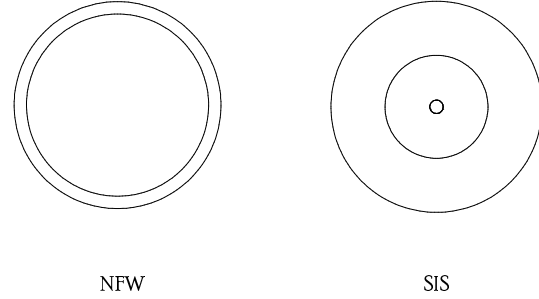


**Fig. 1.** Anatomy of a WIMP clump. Radial distances are drawn on a logarithmic scale, with the center chosen to be  $10^{13}$  cm. The NFW clump (left) shows  $r_c$  inside  $R_{\text{cl}}$ . The SIS clump (right) shows, from inner to outer,  $R_{\text{min}}$ ,  $R_{1/2}$ , and  $R_{\text{cl}}$ . Both clumps are  $10^8 M_\odot$ , with  $R_{\text{cl}} \sim 1$  kpc.

In order to study the range of possible clump radial profiles, we also consider the case of clumps described by singular isothermal spheres (SIS). The density profile in this case is given by:

$$\rho(r) = m_\chi n_0 \left(\frac{r}{r_c}\right)^{-2}. \quad (2)$$

By contrast with NFW, the SIS profile provides a steeper slope, leading to a sharp peak density at the center of the clump. The SIS model describes a collection of self-gravitating collisionless particles. If dark matter clumps lack baryons, then this profile is likely to be more appropriate. The parameters  $r_c$  and  $n_0$  are fixed by the total clump mass and the halo density at the edge. Figure 1 sketches both NFW and SIS clumps ( $R_{\text{min}}$  and  $R_{1/2}$  are described in section 4).

In addition to the specific halo and clump profiles, we need a model for the distribution of clumps in the halo. Following Blasi and Sheth (2000), clumps of mass  $m$  and position  $r$  are distributed according to

$$n_{\text{cl}}(r, m) = n_{\text{cl},0} \left(\frac{m}{M_H}\right)^{-\alpha} \left[1 + \left(\frac{r}{r_c^{\text{cl}}}\right)^2\right]^{-3/2}, \quad (3)$$

where  $n_{\text{cl},0}$  is a normalization constant and  $r_c^{\text{cl}}$  is the core of the clump distribution. A value of  $\alpha \sim 1.9$  fits well the simulations in Ghigna et al. (1998), in which a halo with  $M_H \approx 2 \times 10^{12} M_\odot$  contains about 500 clumps with mass larger than  $M_{\text{cl},\text{min}} \sim 10^8 M_\odot$ . The presence of such dark substructure gains some support from recent analyses of strong gravitational lens systems (see, for example, Chiba (2001)), where dwarf galaxy satellites and globular clusters are insufficient to affect the lensing, but dark subhalo structures do alter the flux ratios in multiply imaged systems.

The halo representations generated here extend the clump distribution to a lower mass cutoff of  $10^7 M_\odot$ . In principle, lower mass clumps will be present in simulations with larger dynamical range. For the case of gamma-ray emission, Calcáneo–Roldán and Moore (2001) find that little additional flux arises if the minimum mass cutoff is lowered. A more detailed study of lower mass clumps will be described in Aloisio et al. (2002b).

## 2.2 Generating Synchrotron Radiation

Neutralinos in DM clumps annihilate mostly into quark-anti-quark pairs which hadronize mostly into pions. The neutral pions give rise to the gamma-ray emission via  $\pi^0 \rightarrow \gamma\gamma$ ; while charged pions decay into charged leptons:

$$\pi^+ \rightarrow \mu^+ \nu_\mu, \quad \pi^- \rightarrow \mu^- \bar{\nu}_\mu, \quad (4)$$

and muons subsequently decay into electrons and positrons:

$$\mu^+ \rightarrow e^+ \bar{\nu}_\mu \nu_e, \quad \mu^- \rightarrow e^- \nu_\mu \bar{\nu}_e. \quad (5)$$

Neutrinos from this cascade process may eventually be detectable, while electrons and positrons can be observed via synchrotron radiation in the presence of magnetic fields.

The number of electrons and positrons produced at each energy resulting from a single  $\chi\bar{\chi}$  annihilation,  $\frac{dN_e}{dE_e}$ , can be calculated via:

$$\frac{dN_e}{dE_e} = \int_{E_e}^{m_\chi c^2} \int_{E_\mu}^{E_\mu/\bar{r}} W_\pi \frac{dN_\mu^{(\pi)}}{dE_\mu} \frac{dN_e^{(\mu)}}{dE_e} dE_\pi dE_\mu, \quad (6)$$

where  $\bar{r} \equiv (m_\mu/m_\pi)^2$  and

$$W_\pi = \frac{15}{16} \left( \frac{E_\pi}{m_\chi c^2} \right)^{-3/2} \left( 1 - \frac{E_\pi}{m_\chi c^2} \right)^2. \quad (7)$$

This form for the pion spectrum is the result of the fragmentation and hadronization of partons, as found in Hill (1983). More sophisticated fits can be used but for the present work eq. (7) is sufficient. It is worth noting the strongly non-thermal form of the fragmentation spectrum, which is instrumental in distinguishing DM annihilation from the background provided by the CMB radiation. In the integral (6), the pion decay generates the following muon number per unit energy:

$$\frac{dN_\mu^{(\pi)}}{dE_\mu} = \frac{1}{E_\pi} \frac{m_\pi^2}{m_\pi^2 - m_\mu^2} \quad (8)$$

and the muon decay gives

$$\frac{dN_e^{(\mu)}}{dE_e} = \frac{2}{E_\mu} \left[ \frac{5}{6} - \frac{3}{2} \left( \frac{E_e}{E_\mu} \right)^2 + \frac{2}{3} \left( \frac{E_e}{E_\mu} \right)^3 \right]. \quad (9)$$

At low energies, eq. (6) behaves as

$$\frac{dN_e}{dE_e} \sim E_e^{-\frac{3}{2}}, \quad (10)$$

and goes to zero as  $E_e$  reaches the maximum energy which is of the order of  $m_\chi$ .

The total injection rate of electrons and positrons by neutralino annihilations is then given by

$$q_e(E_e) = n_\chi^2 \langle \sigma v \rangle_{\chi\bar{\chi}} \left( \frac{dN_e}{dE_e} \right); \quad (11)$$

where  $\langle \sigma v \rangle_{\chi\bar{\chi}}$  is the annihilation rate. Depending on the specific neutralino model, the annihilation rate varies around a fiducial value of  $\langle \sigma v \rangle_{\chi\bar{\chi}} \simeq 3 \times 10^{-29} \text{ cm}^3/\text{s}$ , with a wide spread. The electron-positron population at any point in space can be written as

$$\frac{dn_e}{dE_e} \simeq q_e \tau, \quad (12)$$

where  $\tau$  is the average lifetime of the electron or positron. For the cases considered below, the electron or positron gyroradius is usually much smaller than the size of the emitting region. It is a good assumption to calculate the emission of electrons and positrons as coming from their original position.  $\tau$  is the timescale over which electrons and positrons radiate away most of their energy.

Depending on the density profile of the clump, the electron or positron energy,  $E_e$ , and the position within a clump,  $\tau$  is determined by the shortest among the following timescales: the energy loss timescale for (1) synchrotron radiation, (2) inverse Compton scattering (ICS) off the cosmic microwave background (CMB), (3) ICS off the local synchrotron photons, and (4) the possibility of electron-positron annihilation. In the NFW case discussed below, the synchrotron emission is the main energy loss process. The SIS case has different regimes with the central regions being dominated by ICS off the generated synchrotron photons. We discuss each case in more detail below.

The total synchrotron power (Rybicki and Lightman, 1979),

$$\frac{dE_{\text{syn}}}{dt} = 4 \times 10^{-21} B_\mu^2 E_e^2 \text{ erg/s}, \quad (13)$$

where  $B_\mu$  is the magnetic field strength in  $\mu\text{Gauss}$  and  $E_e$  is the electron energy in GeV. In our Galaxy, estimates of  $B_\mu$  vary between 3 and 6. If we choose  $E_e \sim m_\chi \sim 100 \text{ GeV}$ , the typical synchrotron power becomes  $4 \times 10^{-17} \text{ erg/s}$ . The peak frequency,

$$\nu_{\text{max}} = 3.7 \times 10^6 B_\mu E_e^2 \text{ Hz}, \quad (14)$$

in the Galactic  $\mu\text{Gauss}$  fields, indicate that the synchrotron emission should be observable below about 50-100 GHz.

In the numerical calculations of individual clump signatures discussed below, we model the Galactic magnetic field  $B(r, z)$  using Stanev (1997), where here  $r$  and  $z$  are Galaxy-centered cylindrical coordinates. We also assume for simplicity that the synchrotron radiation is mainly produced at the peak frequency defined above.

If the only significant loss process is the emission of synchrotron radiation, then

$$\tau \simeq \frac{E_e}{dE_{\text{syn}}/dt}. \quad (15)$$

The synchrotron emissivity from annihilating neutralinos is then

$$j_\nu \simeq \frac{dn_e}{dE_e} \frac{dE_e}{d\nu} \frac{dE_{\text{syn}}}{dt} \frac{\text{erg}}{\text{cm}^3 \text{s Hz}}. \quad (16)$$

In some regions of DM clumps, other processes affect the electron-positron number density per energy more strongly than the synchrotron emission. In the SIS case, the most significant process is inverse Compton scattering (ICS) off the generated synchrotron photons. Other effects come from the  $e^+ - e^-$  pair annihilation and synchrotron self absorption. We discuss these as they become relevant in section 4.

### 2.3 Comparing with the CMB

As discussed above, the range of frequencies where synchrotron emission from DM clumps may be observed peaks around  $\sim 40$  GHz  $(m_\chi/100\text{GeV})^2$ . This frequency range is the focus of intensive studies of the structure of cosmic microwave background (CMB) radiation. The CMB signals are well understood and well measured and give the opportunity to search for the DM clump emission. We focus our attention on the band between 10 – 400 GHz, which should be relatively free of contaminating CMB foregrounds (Tegmark et al., 2000), and which is where the most sensitive CMB experiments are planned to operate.

Only highly peaked SIS clumps may reach the levels of the CMB emission. In general, the annihilation signal is comparable in flux to the CMB anisotropies, which are at the level of  $\sim 10^{-5}$  of the CMB. In what follows, we assume that the CMB anisotropies have a blackbody spectrum.

The best spectral data on the CMB come from the COBE FIRAS instrument (Fixsen et al., 1996). The reported uncertainties are of order of 20 kJy  $\text{sr}^{-1}$ , above 68 GHz and only above  $7^\circ$  angular scales. The COBE DMR instrument (Smoot et al., 1992) used 31, 53, and 90 GHz, and found consistent anisotropies (of higher order than dipole) at the  $1.1 \times 10^{-5}$  level, but again on  $7^\circ$  scales. A combined FIRAS and DMR analysis (Fixsen et al., 1997) sets the anisotropy spectrum at about  $5 \times 10^{-5}$  of the cosmic monopole spectrum for these large scales.

Our interest is in pixel sizes typical of upcoming CMB probes. The MAP mission (Hinshaw, 2000) is typically 18 arcmin and the Planck Surveyor (de Zotti et al., 1999) is 5 arcmin, so we choose a nominal pixel size of  $10 \times 10$  arcmin (the smaller the pixel, the brighter the clump, because one can aim at the central cusp where the neutralino annihilations are most rapid). The BOOMERANG (de Bernardis et al., 2000) and MAXIMA-1 (Hanany et al., 2000) experiments employed this resolution, and they report  $2.6 \times 10^{-5}$  fluctuations at  $1^\circ$  (BOOMERANG) and  $1.7 \times 10^{-5}$  at 14.4 arcmin (MAXIMA-1), with both quoted at 150 GHz.

On the lower frequency side, some of the best measurements come from the VLA, probing very small angular scales (where primordial plasma fluctuations become damped during the nonzero timescale of recombination). They report  $2 \times 10^{-5}$  at 8.4 GHz (Partridge et al., 1997; Fomalont et al., 1993).

The VLA measurements compare meaningfully with clumps that appear as point sources. For extended sources, it seems best to blend the various experimental results, keeping in mind the pixel size of interest. Fortunately, for all scales, the data are consistent to within an order of magnitude. We choose  $\Delta I_\nu/I_\nu \simeq 2 \times 10^{-5}$  as the limit for detection of deviations distinct from those inherent in the CMB, with the intended caveat that actual detections made in this way deserve further scrutiny regarding the precision of the CMB blackbody.

Then to summarize, our criteria for clump detection over the CMB are as follows: Between 10 and 400 GHz, the center pixel of the clump (taken to be  $10 \times 10$  arcmin) must exceed  $2 \times 10^{-5}$  times  $I_{\nu, \text{CMB}}$  in the same pixel solid angle.

### 3 NFW Clumps

The NFW density profile, given in eq. 1, has a lower density central cusp when compared with a SIS clump. This makes the NFW case simpler: absorption of synchrotron photons by relativistic electrons is unimportant and  $e^\pm$  pair annihilation occurs on a longer time scale than synchrotron radiation, so it can be ignored as well. We also neglect the presence of any constant density core, as this region is in general too small to be detected.

In order to derive the NFW clump signature, it is sufficient to evaluate the integral for the flux observed on Earth, from a clump at distance  $d$ :

$$I_\nu = \frac{1}{4\pi d^2} \int_0^{R_{c1}} 4\pi r^2 j_\nu dr \frac{\text{erg}}{\text{cm}^2 \text{s Hz}}, \quad (17)$$

using eq. 16. Because  $r_c$  is relatively large ( $\sim 75$  pc for a  $10^8 M_\odot$  clump), NFW clumps will often have observable angular sizes.

The detection of a NFW clump can be made by observing both the spectrum of the synchrotron emission as well as the detail angular profile which is resolvable for NFW clumps. In figure 2, we plot the spectrum of a specific NFW clump with mass  $10^8 M_\odot$  located at Galactocentric coordinates  $[-4, 0, 0]$  kpc (the Sun is at  $[-8.5, 0, 0]$ ), and with the following base properties:  $\langle \sigma v \rangle_{\chi\bar{\chi}} = 3 \times 10^{-29} \text{ cm}^3/\text{s}$  and  $m_\chi = 100$  GeV. The thick line gives this clump's spectrum from its central pixel, and the thin solid line shows the CMB anisotropies (taken as  $2 \times 10^{-5} I_{\nu, \text{CMB}}$ ) in the same pixel solid angle. The other lines show the effect of modifying the mass of the clump by a factor of 10 (dashed line), increasing the cross section by a factor of 100 (dotted line), and changing the neutralino mass by a factor of 10 (dot-dashed line) or a factor of 100 (dot-dot-dashed line). One can see that raising  $m_\chi$  results in a higher cutoff frequency, so that if a bright enough annihilating neutralino clump were observed, its spectral cutoff would immediately reveal  $m_\chi$ . On the other hand, changes to  $M_{c1}$  and  $\langle \sigma v \rangle_{\chi\bar{\chi}}$  are degenerate, so some other means is necessary to distinguish between the two, such as gravitational lensing, or dynamical effects on nearby stars.

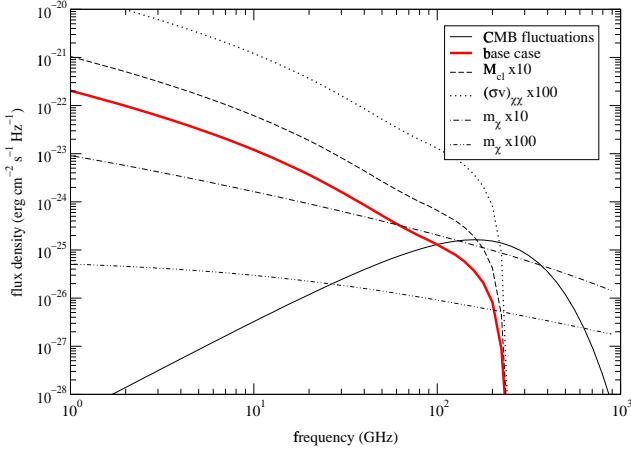


**Fig. 2.** Spectrum of synchrotron emission from an example NFW clump, compared with the CMB anisotropies (thin line) in the same solid angle as the clump. This clump is chosen to lie at Galactocentric coordinates  $[-4, 0, 0]$  kpc, 4.5 kpc away from us. The heavy solid line is the base case, where  $M_{\text{cl}} = 10^8 M_{\odot}$ ,  $\langle\sigma v\rangle_{\chi\bar{\chi}} = 3 \times 10^{-29} \text{ cm}^3/\text{s}$ , and  $m_{\chi} = 100 \text{ GeV}$ . The dashed line increases  $M_{\text{cl}}$  by 10 times; the dotted line increases  $\langle\sigma v\rangle_{\chi\bar{\chi}}$  by 100 times; the dot-dashed line increases  $m_{\chi}$  by 10 times; the dot-dot-dashed line increases  $m_{\chi}$  by 100 times.

We have created several simulations of a clumpy halo. In each, the lower cutoff on the clump mass,  $M_{\text{cl},\text{min}}$ , is a specified parameter. Table 1 presents the major results for each of six halo realizations with  $M_{\text{cl},\text{min}} = 10^7 M_{\odot}$ , for which 3972 clumps were generated, totaling  $\sim \text{few } 10^{11} M_{\odot}$ . These halo simulations all employ base case attributes ( $\langle\sigma v\rangle_{\chi\bar{\chi}} = 3 \times 10^{-29} \text{ cm}^3/\text{s}$  and  $m_{\chi} = 100 \text{ GeV}$ ).

We find that between 250 and 300 clumps will be observable in this halo, above the CMB anisotropies between 10 and 400 GHz as described in section 2.3. None of the NFW clumps is bright enough to outshine the CMB radiation itself; only the CMB fluctuations are exceeded. The NFW clumps in these realizations occupy slightly less than 0.1% of the full sky’s solid angle (assuming a minimum pixel size of  $10 \times 10$  arcmin), and typically several clumps are within 3 kpc of the Earth. (Much of this information in table 1 is

NFW	1	2	3	4	5	6
observable	282	264	289	261	296	265
outshine CMB	0	0	0	0	0	0
$> 30^\circ$ latitude	64	71	59	54	60	68
within 3 kpc	9	8	2	5	5	7
% of sky	0.09	0.06	0.06	0.05	0.07	0.06

**Table 1.** Some results for NFW clumps in six halo realizations, each set with  $M_{\text{cl},\text{min}} = 10^7 M_{\odot}$ , yielding 3972 clumps. The following information on *observable* clumps is given: number of them, number which outshine the CMB (rather than just the CMB anisotropies), number above  $30^\circ$  or below  $-30^\circ$  Galactic latitude, number within 3 kpc of Earth, and the percentage of the sky the clumps occupy.

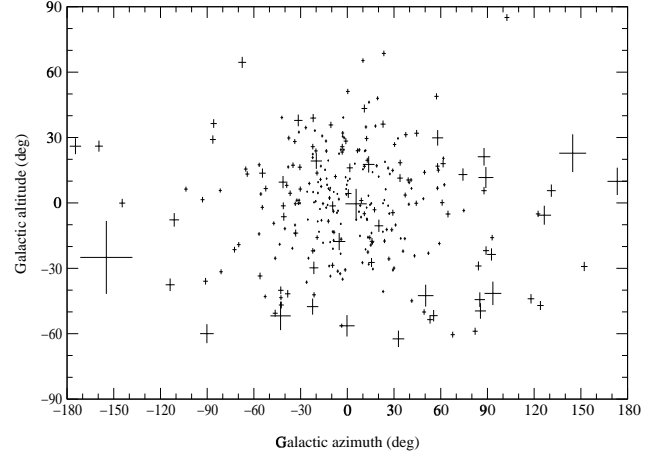


**Fig. 3.** A simulated sky of observable NFW dark matter clumps. Each cross indicates a clump, observable by the criteria laid out in section 2.3. The size of the cross indicates the angular size of the clump such that half its light originates inside the area shown. Angular sizes are exaggerated by a factor of 10.

intended for comparison with the corresponding SIS case, given in table 2 and discussed in section 4.3.)

Of the few hundred observable clumps, between  $\sim 50$  and 75 will reside above  $30^\circ$  or below  $-30^\circ$  Galactic latitude, where Galactic microwave contamination is not problematic. The locations of all the clumps in the sky are depicted for halo realization 1 in figure 3, with crosses indicating the angular size of the clumps such that half of their total emission comes from inside that area. This half-light angle corresponds to a half-light radius, which we will call  $R_{1/2}$ , that equals  $0.26r_c$  for an NFW clump. For clarity, the angular sizes in the figure are exaggerated by a factor of 10.

A histogram of the number of clumps vs. angular size is given in figure 4. The figure shows results for all 6 halo realizations discussed so far, plus several other cases corresponding to modified parameters  $M_{\text{cl},\text{min}}$ ,  $\langle\sigma v\rangle_{\chi\bar{\chi}}$ , and  $m_{\chi}$ ; we modify these in order to cover some of the possible halos and some of the supersymmetric parameter space available to the neutralino. In each case,  $\sim 100$  clumps are resolvable, unless  $m_{\chi}$  is diminished by  $\sim 100$  times which is too small for any reasonable neutralino model. Interestingly, if the clump mass spectrum extends below  $10^7 M_{\odot}$  (in which case there are 23,830 clumps still totaling  $\sim \text{few } \times 10^{11} M_{\odot}$ ), or if  $\langle\sigma v\rangle_{\chi\bar{\chi}}$  is significantly stronger than assumed, many more clumps can be found. A angular correlation function for this case is studied in Aloisio et al. (2002b).

## 4 SIS Clumps

The SIS density profile was given in eq. 2. The steep cusp diverges at the center and makes it necessary to define  $R_{\text{min}}$ , the radius inside which neutralino annihilations are so rapid that  $n_{\chi}(r \leq R_{\text{min}}) = n_{\chi}(R_{\text{min}})$  remains constant.  $R_{\text{min}}$  is found by setting the cusp-forming timescale equal to the

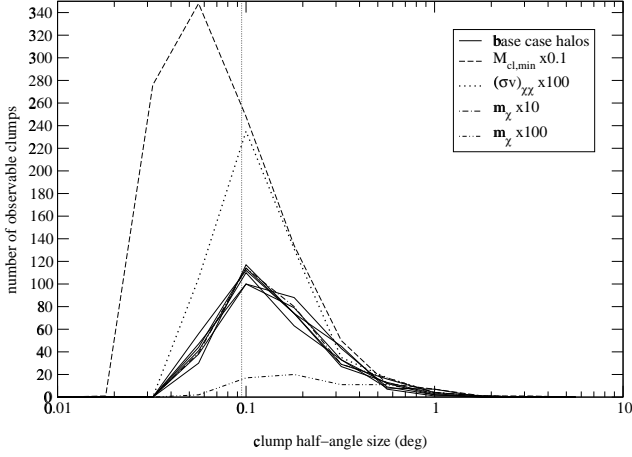


**Fig. 4.** Histogram showing the half-light angular size of NFW clumps in several halo realizations, as used in figure 3. Solid lines are for halo realizations 1 – 6, where  $M_{\text{cl,min}} = 10^7 M_{\odot}$ . The dashed line is for  $M_{\text{cl,min}} = 10^6 M_{\odot}$ ; the dotted line is for  $\langle\sigma v\rangle_{\chi\bar{\chi}}$  increased 100 times; the dot-dashed and dot-dot-dashed lines are for  $m_{\chi}$  increased by 10 and 100 times, respectively. The thin dotted vertical line shows the angular scale of a  $10 \times 10$  arcmin pixel for reference.

$\chi\bar{\chi}$  annihilation timescale (Berezinsky, Gurevich, and Zybin, 1992), so that

$$R_{\text{min}} = R_{\text{cl}} \langle\sigma v\rangle_{\chi\bar{\chi}}^{\frac{1}{2}} \left[ \frac{n_{\text{halo}}}{4\pi G m_{\chi}} \right]^{\frac{1}{4}}, \quad (18)$$

where  $n_{\text{halo}}$  is the halo DM density at the location of the clump.

In the absence of other interactions, one would integrate  $j_{\nu}$  from eq. 16 over the volume of the clump, and find that the dominant part of the flux comes from the vicinity of  $R_{\text{min}}$ . However, due to the high density at the center of an SIS clump, there are other important factors to include. We discuss each factor in turn:

#### 4.1 Relevant Interactions

(1) *Inverse Compton scattering* of electrons and positrons against the synchrotron photons created by the electrons and positrons is the most important correction to the electron-positron distribution in space and energy. To see this, we write the ICS power as (Rybicki and Lightman, 1979)

$$\frac{dE_{\text{ics}}}{dt} = \frac{4}{3} \sigma_T c \beta^2 \gamma^2 U_{\text{ph}}, \quad (19)$$

where  $\sigma_T = 6.65 \times 10^{-25} \text{ cm}^2$  is the Thomson cross section (which is appropriate in the limit  $h\nu \ll m_e c^2$ ),  $\beta \simeq 1$ , and  $U_{\text{ph}}$  is the energy density in the photon field.

The photon population with the greatest energy density controls the rate of ICS. For the CMB,

$$U_{\text{cmb}} = aT_{\text{cmb}}^4, \quad (20)$$

where  $a = 7.56 \times 10^{-15} \text{ erg cm}^{-3} \text{ K}^{-4}$  and  $T_{\text{cmb}} = 2.728 \text{ K}$ . At the inner cores of the SIS clumps, we find that the synchrotron photon population dominates the photon energy density such that  $U_{\text{ph}} \simeq U_{\text{syn}} > U_{\text{cmb}}$ . The synchrotron energy density at distance  $r$  from the clump center can be calculated as the integral of the emissivity along all lines of sight,  $s(r)$ , from  $r$  to all other points in the clump. The energy and space dependence in the equilibrium density of electrons and positrons can be factorized as  $dn_e(E_e, r)/dE_e \propto \sigma_0(r)\Phi(E)$ , following from a similar factorization in the injection function  $q(E_e, r)$ . This leads to

$$U_{\text{syn}}(r) \propto B^2 m_{\chi}^3 I(r) \quad (21)$$

where

$$I(r) = \frac{1}{2} \int_{-1}^1 d\cos\theta \int_0^{s_{\text{max}}} \sigma_0(r(s)) ds, \quad (22)$$

and  $s_{\text{max}} = r\cos\theta + ((r\cos\theta)^2 + R_c^2 - r^2)^{1/2}$ . After some algebraic steps we find that

$$\sigma_0(r) \propto r^{-\beta} / I(r), \quad (23)$$

where  $\beta$  is the slope of the radial dependence in the injection function ( $\beta = 4$  for isothermal clumps outside the minimum radius). The detailed equation is then solved iteratively in order to calculate the equilibrium electron positron function, which gives

$$\frac{dn_e(E_e, r)}{dE_e} \propto E_e^{-5/2} r^{-5/2}, \quad (24)$$

for an isothermal clump. Note that in the most general case that we considered numerically, the equation to solve is an integral equation since the function  $I(r)$  contains the unknown equilibrium distribution.

This holds wherever electron losses are fastest by ICS against the synchrotron photon field. In the case of losses being dominated by synchrotron radiation and ICS against the CMB instead, the loss mechanism is independent of  $r$ , and  $dn_e/E_e \propto E_e^{-5/2} r^{-4}$ . Since the two forms of electron losses have different power laws in  $r$  (and the same power law in  $E_e$ ), there is a transition radius  $R_{\text{ics,syn}}$  (which is independent of  $E_e$ ) between the two behaviors.

(2) *Pair annihilation* between  $e^-$  and  $e^+$  particles would have an important role in determining the flux from a DM source in the absence of the ICS described above. But in the presence of ICS losses, pair annihilation makes little difference to the resulting radio flux. Pair annihilation is still important, because it reduces the population of the lower energy pairs, which would otherwise upscatter photons frequently enough to affect the synchrotron spectrum.

We can estimate the  $e^{\pm}$  lifetime for the case where electrons annihilate before they lose a significant fraction of their original energy via synchrotron or ICS as

$$\tau_{e^{\pm}} \simeq \frac{1}{\langle n_e - \sigma_{e^{\pm}} v_{e^{\pm}} \rangle} \quad (25)$$

with  $v_e \simeq c$ , and the angle brackets indicating an average over  $E_{e-}$ . (This is equally valid if we interchange all the plus and minus signs, but we will keep track of signs in order to distinguish between particles and antiparticles.)

With eq. (12), we have

$$\frac{dn_{e+}}{dE_{e+}} = \frac{q_{e+}}{\langle n_{e-} \sigma_{e\pm} v_{e-} \rangle}. \quad (26)$$

The term in angle brackets is computed from the equations in Svensson (1982) (also consistent with Coppi and Blandford (1990)).  $\langle n_{e-} \sigma_{e\pm} v_{e-} \rangle$  can be expressed as an energy integral which depends on the  $e^\pm$  distribution that we are trying to determine. Again, we find the solution to this non-linear equation via numerical iterations.

Neglecting a slow varying logarithm in the annihilation cross section, one finds that  $n_{e-}$  is roughly constant and  $\langle \sigma_{e\pm} v_{e-} \rangle \propto E_{e+}^{-1}$ . That is, a given positron of any energy sees essentially the same distribution of target electrons, so to a first approximation, it is sufficient to replace the electron distribution with a single population at energy  $E_{e-} \simeq m_e c^2$ . By that rationale,  $\tau_{e+} \sim E_{e+}$ . At low energies where  $dN_e/dE_e \sim E_e^{-3/2}$ , this means that  $dn_e/dE_e \sim E_e^{-1/2}$  and  $n_e \sim E_e^{1/2}$  (where the subscript  $e$  refers to either an electron or a positron).

The distribution in space, rather than energy, is easier to determine. In order to satisfy eq. (26) with the injection  $q_e \propto r^{-4}$  set by the isothermal DM profile, we must have  $dn_e/dE_e \propto r^{-2}$ . Then for a region whose  $e^\pm$  losses are fastest by pair annihilation, we have

$$\frac{dn_e}{dE_e} \propto E_e^{-1/2} r^{-2}. \quad (27)$$

We define  $R_{\text{ann,ics}}$  as the transition radius between the  $r^{-2}$  pair annihilation distribution and the  $r^{-5/2}$  ICS distribution. If  $R_{\text{ann,ics}} > R_{\text{min}}$ , pair annihilation dominates the central region over ICS. In our halo and for most choices of  $m_\chi$ ,  $R_{\text{ann,ics}} < R_{\text{min}}$  for electrons radiating at frequencies of interest. The distribution flattens at the center before the density can get high enough to create a pair annihilation dominated region. At lower frequencies, pair annihilation becomes important and limits the number of low energy pairs which become unable to effect the synchrotron spectrum.

(3) *Synchrotron self absorption* (SSA) occurs when the electrons in the magnetic field can absorb the energy of the synchrotron photons. The per-unit-length absorption coefficient for SSA can be written as:

$$\alpha_\nu = -\frac{c^2}{8\pi\nu} \frac{dE_{\text{syn}}}{dt} \left[ \frac{\partial}{\partial\nu} \left( \frac{1}{\nu} \frac{dn_e}{d\nu} \right) \right], \quad (28)$$

where the photon frequency is related to the electron energy via  $\nu_{\text{max}}$ . SSA absorbers of a particular photon are electrons of similar energy to the original synchrotron emitter which made the photon. As such, SSA is only effective below some  $\nu_{\text{crit}}$ , where the corresponding electrons are more numerous.

The source function for an absorbing source is  $S_\nu = j_\nu/\alpha_\nu$ , and the optical depth is

$$\tau_\nu = \int \alpha_\nu dz, \quad (29)$$

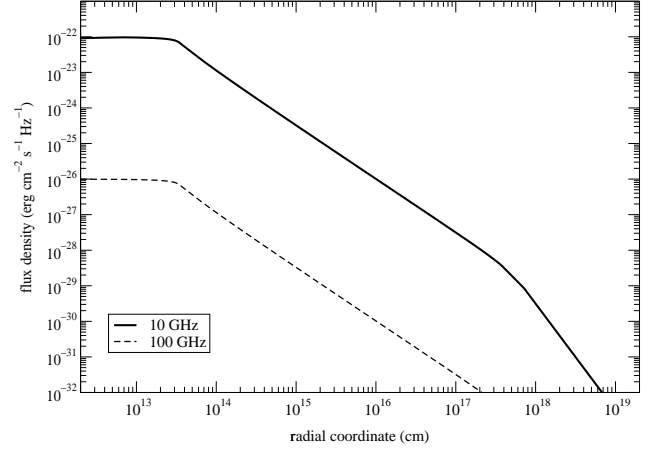


**Fig. 5.** Radial flux profile for an example SIS clump, integrated along the line of sight through the clump. This plot gives the relative intensities found by pointing toward different parts of the clump, given sufficient angular resolution. The solid line is for 10 GHz and the dashed line is for 100 GHz.

where  $z$  is a line-of-sight coordinate. The flux density from such a source at distance  $d$  from the Earth is obtained by summing over each line of sight through the DM clump:

$$I_\nu = \frac{1}{4\pi d^2} \int_0^{R_{\text{cl}}} 2\pi b S_\nu (1 - e^{-\tau_\nu}) db \frac{\text{erg}}{\text{cm}^2 \text{s Hz}}. \quad (30)$$

The SSA cutoff frequency  $\nu_{\text{crit}}$  depends in part on the absorber density, and without ICS or  $e^\pm$  pair annihilation effects, SSA would be the most important correction to the calculated flux. SSA has been included in the calculations performed here, but since the central absorber population is diminished by ICS, it is of secondary importance.

## 4.2 Results

The synchrotron spectrum of DM clumps is predominantly altered by ICS off synchrotron photons. Figure 5 shows an example of a SIS clump profile that shows the flattened central region. A characteristic size for the clump,  $R_{1/2}$ , can be defined by the radius inside which half of the synchrotron radiation originates.

Figure 6 shows the spectrum of synchrotron emission from a SIS clump in the same position as the NFW clump of figure 2. The thick solid line gives the base case,  $M_{\text{cl}} = 10^8 M_\odot$ ,  $\langle \sigma v \rangle_{\chi\bar{\chi}} = 3 \times 10^{-29} \text{ cm}^3/\text{s}$ , and  $m_\chi = 100 \text{ GeV}$ . The dashed line increases  $M_{\text{cl}}$  by 10; the dotted line increases  $\langle \sigma v \rangle_{\chi\bar{\chi}}$  by 100 times; the dot-dashed line increases  $m_\chi$  by 10 times; the dot-dot-dashed line increases  $m_\chi$  by 100 times. The thin solid line gives the intensity of the CMB within the  $10 \times 10$  arcmin pixel, for comparison.

In order to compare the SIS with the NFW clumps, we used the same halo simulations as in the NFW case: realizations 1 – 6 with 3972 clumps ( $M_{\text{cl,min}} = 10^7 M_\odot$ ), and another realization with 23,830 clumps ( $M_{\text{cl,min}} = 10^6 M_\odot$ ), all with  $\sim \text{few} \times 10^{11} M_\odot$  total. For a typical clump mass of

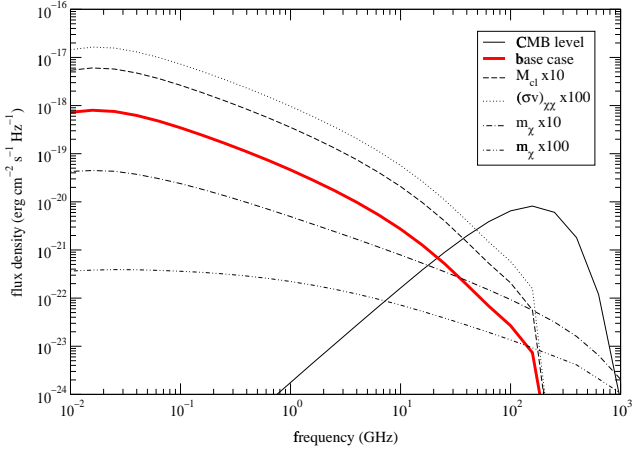


**Fig. 6.** Spectrum of synchrotron emission from an example SIS clump chosen to lie at Galactocentric coordinates  $[-4, 0, 0]$  kpc. The thick solid line gives the base case,  $M_{\text{cl}} = 10^8 M_\odot$ ,  $\langle\sigma v\rangle_{\chi\bar{\chi}} = 3 \times 10^{-29} \text{ cm}^3/\text{s}$ , and  $m_\chi = 100 \text{ GeV}$ . The dashed line increases  $M_{\text{cl}}$  by 10 times; the dotted line increases  $\langle\sigma v\rangle_{\chi\bar{\chi}}$  by 100 times; the dot-dashed line increases  $m_\chi$  by 10 times; the dot-dot-dashed line increases  $m_\chi$  by 100 times. The thin solid line gives the intensity of the CMB within the  $10 \times 10$  arcmin pixel, for comparison.

$10^8 M_\odot$ , a SIS clump can outshine a NFW clump by about  $10^5$  times in the microwave.

The visible SIS clumps for halo realization 1 are shown in figure 7, here with angular sizes based on  $R_{1/2}$  exaggerated by a factor of 5,000 (none of these clumps is resolvable without interferometry). In table 2, we list some results of the SIS case. First, we find that SIS clumps (in an NFW halo) tend to produce 600 – 700 observable sources, which is a few times more than the NFW clump case (compare tables 1 and 2). The combined sources occupy only slightly less solid angle than with NFW, mostly due to the small angular size of SIS clumps. But unlike the NFW case,  $\sim 20\%$  of the SIS clumps not only outshine the CMB anisotropies, but outshine the CMB altogether. A similar percentage of observable clumps is located outside the direction of the Galactic disk. Finally, the table gives several observable clumps within 3 kpc of the Earth, which can be resolved (as in figure 5) by long baseline interferometers.

Table 3 gives a comparison of the NFW and SIS clump profiles, by reporting the number of observable clumps in each case, while also varying  $m_\chi$ ,  $\langle\sigma v\rangle_{\chi\bar{\chi}}$ , or  $M_{\text{cl},\text{min}}$ . The results show that changing these parameters has different outcomes for NFW and SIS. For example, increasing  $m_\chi$  by a factor of 100 lowers the spectrum for most relevant  $\nu$  bands (see figure 2); therefore, NFW clumps get dimmer and fewer are seen. On the other hand, the SIS clumps are bright enough to avoid that worry, and the increase in  $m_\chi$  also increases the maximum electron energy. This allows strong sources even in weak magnetic fields via eqs. 13 and 14, raising the number of observable clumps.

As another example, changing  $\langle\sigma v\rangle_{\chi\bar{\chi}}$  has little effect on SIS clumps, because they have an overdensity of electrons

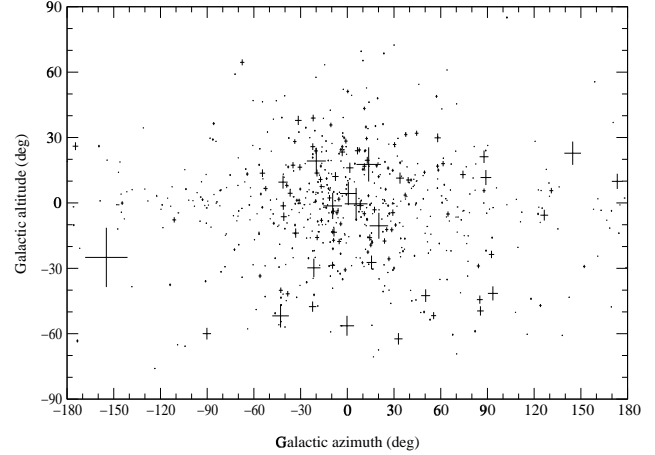


**Fig. 7.** A simulated sky of observable SIS dark matter clumps. Each mark indicates a clump, observable by the criteria laid out in section 2.3. The size of the cross indicates the angular size of the clump such that half its light originates inside the area shown. Angular sizes are exaggerated by a factor of 5000.

and positrons emitting anyway. But for NFW, where the clumps are typically near the CMB anisotropy level, changing the  $\chi\bar{\chi}$  cross section affects the fluxes significantly. Both NFW and SIS cases see similar growth in the number of observable clumps when the clump mass spectrum is extended downward.

## 5 Conclusion

In this paper, we studied the synchrotron signature of neutralino annihilation in the presence of the Galactic magnetic field. If hierarchical CDM clustering extends down to mass scales smaller than dwarf galaxies, these DM clumps are detectable in microwaves over the fluctuations in the CMB.

If the clumps have nearly NFW profiles like the Galaxy, then the clumps have finite angular sizes. NFW clumps have

SIS	1	2	3	4	5	6
observable	636	632	676	656	682	616
outshine CMB	54	34	38	37	37	40
> 30° latitude	130	155	144	129	140	135
within 3 kpc	9	8	2	5	5	7
resolvable	212	184	209	190	210	201
resolve > 30°	48	53	51	49	54	59
% of sky	0.04	0.04	0.05	0.04	0.05	0.04

**Table 2.** Some results for SIS clumps in six halo realizations, each set with  $M_{\text{cl},\text{min}} = 10^7 M_\odot$ , yielding 3972 clumps. The following information on *observable* clumps is given: number of them, number which outshine the CMB (rather than just the CMB anisotropies), number above 30° (or below  $-30^\circ$ ) Galactic latitude, number within 3 kpc of Earth, number resolvable by 10 km interferometry such as the VLA, number resolvable by the VLA above 30° Galactic latitude, and the percentage of the sky the clumps occupy.

case	NFW	SIS
base case	282	636
$\langle\sigma v\rangle_{\chi\bar{\chi}} \times 100$	528	671
$m_{\chi} \times 10$	284	1126
$m_{\chi} \times 100$	66	917
$M_{\text{cl},\text{min}} \times 0.1$	1078	3503

**Table 3.** Comparison of NFW and SIS clumps. The base case refers to  $m_{\chi} = 100$  GeV,  $\langle\sigma v\rangle_{\chi\bar{\chi}} \simeq 3 \times 10^{-29}$  cm<sup>3</sup>/s, and  $M_{\text{cl},\text{min}} = 10^7 M_{\odot}$ . The other cases modify these parameters as stated. The last row of the table uses a different halo realization than the other rows.

synchrotron spectrum from non-thermal electrons with negligible ICS and self-absorption. NFW clumps will be large enough and numerous enough that several should be resolvable in angular profile by CMB anisotropy experiments. The light profile will follow  $r^{-1}$  inside a core radius. The statistics of the clumps distribution should be consistency with figure 4 and table 1.

SIS clumps are brighter and smaller in angular size. The clumps have a distinctive spectrum due to a combination of ICS and pair annihilation features, in a particular radial structure. The spectrum can be checked at lower frequencies also, because these clumps are very bright and may outshine other radio backgrounds. A few clumps should be close enough to display a distinctive radial profile by interferometric means.

In either case, one should make use of CMB anisotropy studies to search for neutralino annihilation in DM clumps. Many clumps should have signal above  $2 \times 10^{-5}$  times the 2.728 K Planck function. The sources are usually small and occupy a small fraction of the sky, so that a full sky high resolution microwave survey maybe necessary. The upcoming MAP and Planck missions will provide that. Even in smaller data sets such as the BOOMERANG, MAXIMA, and DAS1, it is possible that clumps can be detected.

Upon finding synchrotron source clumps or hot pixels, one final check can prove their DM nature. The gamma ray and neutrino emission from them must fit the expected levels, and must be independent of position in the Galaxy, unlike the synchrotron which follows the Galaxy’s magnetic field. This combination of signatures makes the sources unique, and aids in extracting specific information about them:  $M_{\text{cl}}$ ,  $m_{\chi}$ , and  $\langle\sigma v\rangle_{\chi\bar{\chi}}$ .

One interesting point to note is that for reasonable choices of the appropriate parameters, we find that several hundred or more clumps are typically observable in either profile. If new CMB experiments fail to detect them, then we have learned that either neutralinos are not the dark matter, or CDM halo clumps do not exist. However, if they are found, they offer a valuable opportunity to learn more about CDM clustering, neutralino properties like mass and cross section, and possibly the Galactic magnetic field structure.

*Acknowledgements.* This work was supported in part by the NSF through grant AST-0071235 and DOE grant DE-FG0291-ER40606 at the University of Chicago and at the Center for Cosmological

Physics by grant NSF PHY-0114422.

## References

- Aloisio, R., Blasi, P., Olinto, A.V., in preparation.  
Aloisio, R., Blasi, P., Olinto, A.V., Tasitsiomi, A., in preparation.  
Berezinsky, V., Gurevich, A.V., and Zybin, K.P., Phys. Lett. B 294, 221, 1992.  
Berezinsky, V., Bottino, A., and Mignola, G. Phys. Lett. B 325, 136, 1994.  
Bergström, L., Edsjö, J., Gondolo, P., Ullio, P., Phys. Rev. D 59, 043506, 1999.  
de Bernardis, P. et al. (BOOMERANG collaboration), Nature 404, 955, 2000; de Bernardis, P. et al., astro-ph/0011469.  
Blasi, P., and Sheth, R. K., Phys. Lett. B 486, 233, 2000.  
Calcáneo-Roldán, C. and Moore, B., astro-ph/0010056.  
Chiba, M., astro-ph/0109499.  
Coppi, P.S. and Blandford, R.D., MNRAS 245, 453, 1990.  
Fixsen, D.J., Cheng, E.S., Gales, J.M., Mather, J.C., Shafer, R.A., Wright, E.L., Ap. J. 473, 576, 1996.  
Fixsen, D.J., Hinshaw, G., Bennett, C.L., Mather, J.C., Ap. J. 486, 623, 1997.  
Fomalont, E.B., Partridge, R.B., Lowenthal, J.D., Windhorst, R.A., Ap. J. 404, 8, 1993.  
Ghigna, S., Moore, B., Governato, F., Lake, G., Quinn, T., Stadel, J., MNRAS 300, 146, 1998.  
Gondolo, P., preprint hep-ph/0002226.  
Gondolo, P. and Silk, J., Phys. Rev. Lett. 83, 1719, 1999.  
Hanany, S. et al., Ap. J. 545, L5, 2000.  
Hill, C.T., Nucl. Phys. B224, 469 (1983).  
Hinshaw, G., astro-ph/0011555.  
Jungman, G., Kamionkowski, M., and Griest, K., Phys. Rep. 267, 195, 1996.  
Navarro, J.F., Frenk, C.S., and White, S.D.M., Ap. J. 462, 563, 1996; ibid. 490, 493, 1997.  
Partridge, R.B., Richards, E.A., Fomalont, E.B., Kellerman, K.I., Windhorst, R.A., Ap. J. 483, 38, 1997.  
Rybicki, G.B. and Lightman, A.P., “Radiative Processes in Astrophysics”, 1979.  
Salucci, (2000).  
Smoot, G.F. et al. (COBE DMR collaboration), Ap. J. 396, L1, 1992.  
Stanev, T., Astrophys. J. 479, 290, 1997.  
Svensson, R., Ap.J. 258, 321, 1982.  
Tegmark, M., Eisenstein, D.J., Hu, W., and de Oliveira-Costa, A., Ap.J. 530, 133, 2000.  
Tyler, C., in preparation.  
de Zotti, G. et al., astro-ph/9902103.